Impact of intermolecular non-covalent interactions in a CuI8PdII1 discrete assembly: conformers' geometries and stimuli-sensitive luminescence properties

Florent Moutier, Jana Schiller, Constance Lecourt, Ali Moustafa Khalil, Vincent Delmas, Guillaume Calvez, Karine Costuas, Christophe Lescop

Impact of intermolecular non-covalent interactions in a $Cu^{I}_{8}Pd^{II}_{1}$ discrete assembly: conformers' geometries and stimuli-sensitive luminescence properties.

Florent Moutier, Jana Schiller, Constance Lecourt, Ali Moustafa Khalil, Vincent Delmas, Guillaume Calvez,* Karine Costuas,* and Christophe Lescop*

[a] Mr. F. Moutier, Dr. J. Schiller, Dr. C. Lecourt, Dr. A. Khalil, Dr. V. Delmas, Dr. G. Calvez, Dr. K. Costuas, Dr. C. Lescop
Univ Rennes, INSA Rennes, CNRS, ISCR – UMR6226, F-35000 Rennes, France
E-mail: guillaume.calvez@insa-rennes.fr, karine.costuas@univ-rennes1.fr, christophe.lescop@insa-rennes.fr

Supporting information for this article is given via a link at the end of the document.

Abstract: A new highly solid-state luminescent phase of a previously reported weakly luminescent $Cu^{I}_{8}Pd^{II}_{1}$ dicationic assembly is reported revealing the high geometrical versatility of this moiety that importantly alters its luminescent properties. This very minor new species $\mathbf{B_c}$ is based on a different conformer scaffold than the one encountered in the previously reported $\mathbf{B_o}$ form and, essentially differs from $\mathbf{B_o}$ by displaying shorter Cu^{I}-Cu^{I} intermetallic distances. DFT calculations allow concluding that the predominance in the solid-state of the weakly luminescent and less stable $\mathbf{B_o}$ phase is due to the extra stability induced by a larger number of intermolecular non-covalent π-CH interactions in its crystalline packing and not by the intrinsic stability of the $Cu^{I}_{8}Pd^{II}_{1}$ dicationic moiety. Calculations also revealed that a more stable conformation $\mathbf{B_{calc}}$ is expected in vacuum, which bears a different distribution of Cu^{I}-Cu^{I} intermetallic distances than the dications in $\mathbf{B_o}$ and $\mathbf{B_c}$ phases. Taking into account that the geometrical alterations are associated to drastic changes of luminescence properties, this confer to the $Cu^{I}_{8}Pd^{II}_{1}$ assembly high potentiality as stimuli-sensitive luminescent materials. Indeed, by applying mechanical or thermal stress to samples of $\mathbf{B_o}$ phase, new phases $\mathbf{B_g}$ and $\mathbf{B_m}$, respectively, were obtained. Alterations of the solid-state photophysical properties of these new species compared to those recorded for $\mathbf{B_o}$ are reported together with a combined experimental and computed study of the structures/properties relationships observed in these phases.

Introduction

The recent development in science and technology targeting photofunctional molecular materials have highlighted for such derivatives appealing perspectives in manifold fields including organic light emitting diodes,[1] solar cells,[2] luminescent sensors,[3] or anti-counterfeiting,[4] just to name a few. Among these materials, an ever-growing number of stimuli-responsive luminescent sensors has been reported, comprising rich thermo-, mechano-, vapo- or solvato-chromic luminescence properties. Regarding more specifically mechanochromic derivatives,[5] the color of the light emitted by the luminescent material is altered upon application of a mechanic stress. The mechanisms at the origin of such properties changes are generally ascribed to stimuli-induced transformations of structural arrangements and/or packing modes (molecular conformations and/or intermolecular interactions) in the solid-state, that concomitantly impact the electronic structures and solid-state photophysical properties. In this context, the rationalization of the way intermolecular or intramolecular non-convalent interactions between emissive centers can be modified in the solid-state carries a paramount importance in order to design, understand, optimize and control the mechanochromic response of luminescent molecular materials.

So far, in the field of mechanochromic materials, the majority of systems that have been reported are organic dyes[5a,6] and gold[7a-k] and platinum[7l-r] metal-based compounds[5b] which show a rich variety of mechanochromic properties. In this field, the development of mechanochromic luminescent Cu^{I} coordination complexes offers particularly appealing perspectives for upcoming developments not only because of the low cost and relatively high abundance of copper but also due to the fascinating and various photophysical properties these complexes can exhibit.[5b,8,9,10] The emission behaviors of Cu^{I} complexes are indeed characterized by the large diversity of the radiative relaxation processes involved with a rising attention being paid to derivatives exhibiting Thermally Activated Delayed Fluorescence (TADF).[8f,g, 9] In such complexes, spatially well-separated HOMO and LUMO orbitals induce small lowest energy singlet-triplet energy gap. This can allow thermal population of the lowest energy excited singlet state (S_1) from the lowest energy triplet excited state (T_1), via a reverse intersystem crossing (RISC) inducing efficient radiative relaxation to the ground state and exalted solid-state luminescence properties that occurs ideally at temperatures close to room temperature (RT). Importantly, this phenomenon is not only observed for mononuclear Cu(I) complexes but several polynuclear Cu^{I} complexes have been also reported with enhanced solid-state luminescent properties.[5b, 9n-x, 10d-j] In such derivatives non-covalent short intermetallic cuprophilic interactions (d(Cu-Cu) bellow ca. 2.9 Å)[11] can be found in the ground state and/or in the excited states relaxed geometries.[9t,u] Such interactions induce a significant enhancement of the spin-orbit coupling (SOC) constants compared to the one induced by the presence of non-interacting Cu^{I} ions for which intrinsic individual SOC is generaly moderate. Consequently, radiative rates constants for the T_1 states are increased, promoting efficient RISC to the S_1 states but also fast and efficient phosphorescent relaxation process to the ground states (S_0).

While luminescent Cu^{I} derivatives focused so far a great attention for the preparation and study of innovative emitters in OLEDs,[8f,9] these systems also deserve interest as new sources of stimuli responsive multifunctional luminescent materials.[10] Indeed, the Cu^{I} ion presents a coordination sphere characterized

by a high degree of flexibility and lability which renders the gross conformation of Cu^{I} species very sensitive to external stimuli, and concomitantly impacts their photophysical properties. In this context, Perruchas *et al.* have extensively studied in the recent years the mechanochromic responses of a series of copper iodide clusters mostly based on Cu_4I_4 cubane units stabilized by various phosphine ligands.[5b,12] Using a variety of solid-state characterization techniques including Powder X-Ray Diffraction (PXRD), solid state ^{63}Cu and ^{31}P NMR, solid-state IR and Raman spectroscopies, these studies have allowed to assign the origin of the mechanochromic properties to modifications of the intermetallic cuprophilic interactions as a result of the application of a mechanical stress. It was revealed that such stress induces a transition from crystalline to a partially amorphous state in which intermolecular contacts in the crystal packing are likely to be altered. As a result, the molecular geometries can relax to an energetically more favored conformation than the one stabilized in the single crystals. Indeed, in such mechanically induced phases, individual molecules are released from some of the stabilizing intermolecular packing non-covalent interactions whose accumulation can impose specific molecular conformations. Similarly, Chen *et al.* and Jin *et al.* recently reported luminescent Cu^{I} derivatives whose mechanochromic properties are assigned to π-π interactions or hydrogen bonds alteration upon grinding from the pristine crystalline phases to the grinded amorphous phases, supporting the crucial importance of intermolecular interactions in the solid-state to control stimuli-responsive luminescence properties.[13] Artem'ev *et al.* also recently described the first Cu^{I} trimers reported to date to be stabilized by triply bridging phosphine ligand in which the mechanochromic behaviors observed are assigned by the authors to the crystalline to amorphous phase transition and concomitant local molecular geometry reorganizations.[14]

Herein, we report firstly the polymorphic behavior of a luminescent $[Cu_8Pd_1(CN)_8dppm_8](PF_6)_2$, thereafter named $Cu^{I}_8Pd^{II}_1$, discrete polymetallic assembly (dppm = 1,1-bis(diphenylphosphino)methane). While the 'open-form' $\mathbf{B_o}$ was initially reported as being the only phase obtained upon crystallization, we have observed recently the formation upon the same crystallization conditions of traces of a 'closed-form', $\mathbf{B_c}$ (scheme 1). X-ray crystal structure resolution reveals that $\mathbf{B_c}$ is a conformational isomer of $\mathbf{B_o}$ in which intermetallic Cu^{I} distances are significantly shorter as a result of different coordination mode of internal cyanide ligands (μ^3 in $\mathbf{B_c}$ versus μ^2 in $\mathbf{B_o}$). Photophysical properties of $\mathbf{B_c}$ reveal a strong enhancement of the radiative relaxation processes and a red-shift of the emission spectra in $\mathbf{B_c}$ compared to those observed in $\mathbf{B_o}$. Attempting to rationalize the preferential formation of $\mathbf{B_o}$ rather than $\mathbf{B_c}$, DFT geometry optimizations of the $Cu^{I}_8Pd^{II}_1$ scaffold were performed by freezing the Cu atomic positions in their crystallographic configurations. It revealed that the conformer $Cu^{I}_8Pd^{II}_1$ in $\mathbf{B_c}$ minor product is more stable than the one characterized in $\mathbf{B_o}$. This led to assign the preferred crystallization of the energetically unfavored $\mathbf{B_o}$ phase to the specific columnar packing encountered in the single crystals of $\mathbf{B_o}$ It provides indeed an accumulation of stabilizing intermolecular non-covalent interactions that is much important than in the $\mathbf{B_c}$ phase packing arrangement. Importantly, non-constrained DFT geometry optimizations revealed that the most stable molecular structure in vacuum, namely the $Cu^{I}_8Pd^{II}_1$ $\mathbf{B_{calc}}$ scaffold, presents a different conformation than the ones found in $\mathbf{B_o}$ and $\mathbf{B_c}$. Compared to the molecular backbones of $\mathbf{B_o}$ and $\mathbf{B_c}$, $\mathbf{B_{calc}}$ scaffold is characterized by a lower symmetry in which the intermetallic Cu^{I} distances are different resulting from alternative set of coordination modes of the internal cyanide ligands. The electronic structures and thus the photophysical properties are concomitantly impacted by the conformation adopted. Taking these results into consideration, a responsive luminescence behavior was anticipated via stimuli that could alter the intermolecular arrangements in the solid-state. We thus performed mechanical treatments of polycrystalline samples of $\mathbf{B_o}$ by grinding, resulting in a partially-amorphized solid $\mathbf{B_g}$ phase. As a result of the applied mechanical stress, local ruptures of the long-range non-covalent interactions that stabilize this conformer in the crystalline state are assumed, allowing some $Cu^{I}_8Pd^{II}_1$ assemblies in the bulk to relax to a more energetically favored conformer which structural parameters are likely to be closer to those of $\mathbf{B_{calc}}$. Finally, by heating solid-state batches of the $\mathbf{B_o}$ phase was also achieved an irreversible melting transition which leads to the amorphous material $\mathbf{B_m}$. Both $\mathbf{B_g}$ and $\mathbf{B_m}$ reveal altered photophysical properties compared to $\mathbf{B_o}$.

Results and Discussion

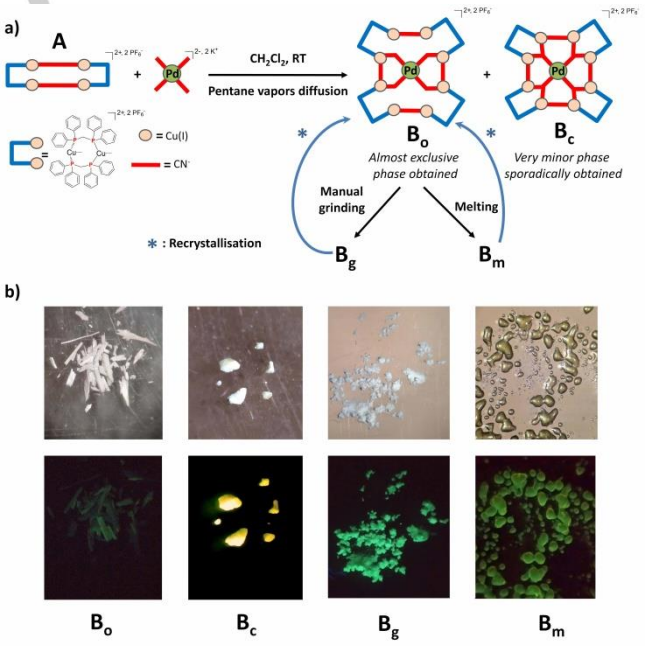

Scheme 1. a) Preparation of the species $\mathbf{B_o}$, $\mathbf{B_c}$, $\mathbf{B_g}$ and $\mathbf{B_m}$; b) Photographs of each sample under visible light (top) and UV-vis light (λ_{ex} = 365 nm, bottom); Photographs of $\mathbf{B_c}$ sample have been taken with a magnification roughly ten-fold larger than those that chosen for the views of $\mathbf{B_o}$, $\mathbf{B_g}$ and $\mathbf{B_m}$ samples.

We have previously reported that the pre-assembled solid-state blue luminophore tetrametallic metallacycle **A**[9t] (Scheme 1), based on the connection of two $[Cu_2(\mu_2\text{-dppm})_2]$ dicationic units with two bridging cyanide ligands, can behave as a very versatile precursor. By reacting it with various pseudo-halide ions (cyanido CN^-, dicyanamide $N(CN)_2^-$ or azido N_3^- ions), a variety of polymetallic Cu^{I} derivatives has been prepared

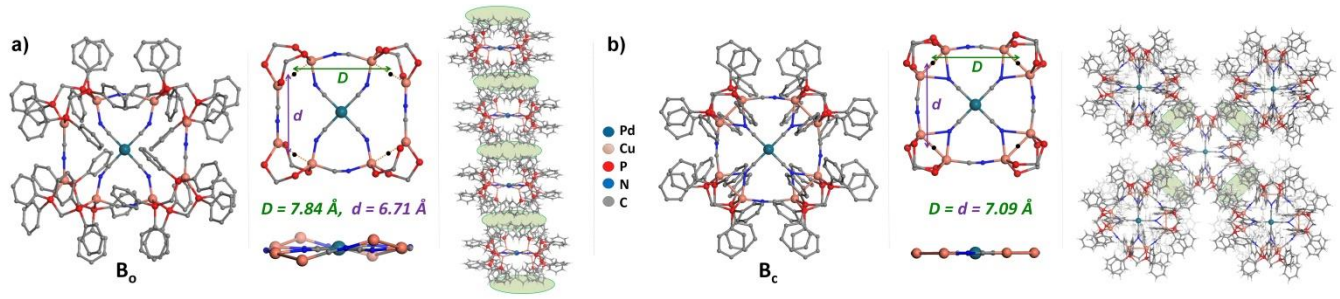

Figure 1. a) Molecular X-ray structure, simplified 'top' and side views of the species **Bo**[15] and view of the columnar solid-state stacking of the derivative **Bo**, b) Molecular X-ray structure, simplified 'top' and side views of the species **Bc** and view of the solid-state stacking mode of the derivative **Bc** (counteranions, H atoms and solvent molecules have been omitted for clarity, location of the C and N atoms of the cyano ligands has been chosen arbitrarily in the X-ray structure views excepted for the $M(CN)_4$ fragments; green coloured ellipses represent the intermolecular π-CH non-covalent interactions areas between neighbouring molecules in the crystal packings; black dots represent the central points of the Cu-Cu segments of each $[Cu_2(\mu_2\text{-dppm})_2]$ fragments).

accordingly to an adapted coordination-driven supramolecular synthetic strategy.[15,16] These derivatives present a variety of molecular structure and luminescence properties due to the versatile photophysical processes and the remarkable conformational flexibility (variation of the intermetallic Cu(I)-Cu(I) distances and of the bite angle of the dppm ligands) lying in the $[Cu_2(\mu_2\text{-dppm})_2]$ building blocks. In particular, we have characterized that the straightforward reaction of two equivalents of **A** with one equivalent of the $[Pd(CN)_4]^{2-}$ metallo-ligand affords (Scheme 1) in the solid-state the $Cu^{I}_8Pd^{II}_1$ assembly in good yield as the room temperature (RT) weakly luminescent $\mathbf{B_o}$ phase.[15] For the sake of the analysis and comparison of the results described herein, structural and photophysical parameters of this previously published[15] polymetallic discrete assembly will be shortly first detailed. Derivative $\mathbf{B_o}$, that can be isolated in a good yield (ca. 70 %) accordingly to the previously published synthetic procedure,[15] crystallizes in the $P2_1/n$ space group of the monoclinic system. This derivative can be described as resulting of the connection of four $[Cu_2(\mu_2\text{-dppm})_2]^{2+}$ fragments with four μ_2-ditopic 'external' cyanido ligands forming a ''$Cu_8(CN)_4$'' metallacycle sub-unit having a slightly twisted rectangular shape (Figure 1a).[17] The backbone of the derivative $\mathbf{B_o}$ results of the connection of this Cu_8 metallacyclic unit to a square planar '$Pd(CN)_4$' internal fragment. Importantly, within the Cu_8 metallacycle sub-unit, the four 'internal' cyanido ligands present a slightly bended μ_2 coordination mode (N≡C-Cu = ca. 168 °). This coordination mode induces an asymmetry of the $[Cu_2(\mu_2\text{-dppm})_2]^{2+}$ fragments with one Cu^{I} metal center presenting a $P_2N_1(C/N)_1$ distorted tetrahedral coordination sphere while the other Cu^{I} metal center has a $P_2(C/N)_1$ distorted trigonal planar coordination sphere.[17] The intermetallic Cu^{I}-Cu^{I} distances in the $[Cu_2(\mu_2\text{-dppm})_2]^{2+}$ sub-units (ca. 3.40 Å) in $\mathbf{B_o}$ are too large for metallophilic interactions. In the solid state, polycrystalline sample of the derivative $\mathbf{B_o}$ displays upon excitation at 350 nm a weak RT greenish luminescence characterized by a broad and featureless band with emission maximum λ_{em} centered at 500 nm. The emissive lifetime τ is 12 μs at 298 K and the emission quantum yield (EQY) is 2 % (Table 1). Upon stepwise cooling in the solid state the emission spectra (λ_{ex} = 350 nm) of derivative $\mathbf{B_o}$ present gradual red-shifts associated with emergence of an intense solid state yellow-green luminescence at low temperature (λ_{em} = 515 nm at 80 K ($\Delta\lambda_{em(298K/80K)}$ = 0.108 eV / 870 cm^{-1})). Concomitantly, the thermal dependence of the emission decay lifetime τ of $\mathbf{B_o}$ in the solid state presents a sigmoidal profile with a τ value of ca. 3 μs at 400 K and a low temperature (80 K) τ value of 222 μs.

While the large majority of the crystallization experiments (conducted at RT upon pentane vapor diffusions within CH_2Cl_2 solutions) exclusively afforded in high yield colorless and weakly RT luminescent needle-shaped crystals of the $\mathbf{B_o}$ phase, we observed sporadically a very few amount of tiny colorless prism-shaped crystals of the new phase $\mathbf{B_c}$ that display at RT an intense eye-perceived yellow luminescence (seen under UV-vis lamp light excitation, λ_{ex} = 365 nm). By repeating in a large number these crystallization experiments, it was possible to collect manually first a single crystal suitable for X-ray crystal structure determination[18] and in a second step sufficiently enough solid-state polycrystalline material[19] to allow the photophysical studies of $\mathbf{B_c}$. The phase $\mathbf{B_c}$ crystallizes in the *I422* space group of the tetragonal system. The unit cell of single crystals of $\mathbf{B_c}$ is composed of a quarter of a dicationic $Cu_8Pd_1(CN)_8dppm_8$ polymetallic assembly, one half of a PF_6^- counter-anion and one included CH_2Cl_2 solvent molecule. The comparison between the X-ray crystal structure resolutions reveals that the dicationic $Cu_8Pd_1(CN)_8dppm_8$ species in $\mathbf{B_c}$ is a conformational isomer of the one observed in $\mathbf{B_o}$ (Figure 1b). Indeed, $Cu^{I}_8Pd^{II}_1$ in $\mathbf{B_c}$ similarly than $Cu^{I}_8Pd^{II}_1$ in $\mathbf{B_o}$ can be described as resulting of the insertion of a square planar '$Pd(CN)_4$' internal fragment within a ''$Cu_8(CN)_4$'' metallacycle sub-unit (Figure 1b) resulting of the connection of four $[Cu_2(\mu_2\text{-dppm})_2]^{2+}$ fragments with four μ_2-ditopic 'external' cyanido ligands. Note that the ''Cu_8'' metallacycle sub-unit is strictly planar in the $\mathbf{B_c}$ scaffold (Figure 1b) which is not the case in the $\mathbf{B_o}$ scaffold. The main structural difference between the solid-state structures of $\mathbf{B_c}$ and $\mathbf{B_o}$ lies in the coordination modes adopted by the four 'internal' cyanido ligands: these cyanide ligands connect in $\mathbf{B_c}$ the central Pd^{II} metal center to all the eight peripheral Cu^{I} metal centers resulting in a symmetrical μ_3 coordination mode (versus a slightly bended μ_2 coordination mode in $\mathbf{B_o}$). Therefore, the overall molecular structure of the phase $\mathbf{B_c}$ (Figure 1b) is more symmetrical than $\mathbf{B_o}$ (Figure 1a) with all the Cu^{I} metal centers having a similar $P_2N_1(C/N)_1$ distorted tetrahedral sphere.[17] In addition, and importantly, in the species $\mathbf{B_c}$, the intermetallic distances within the bimetallic

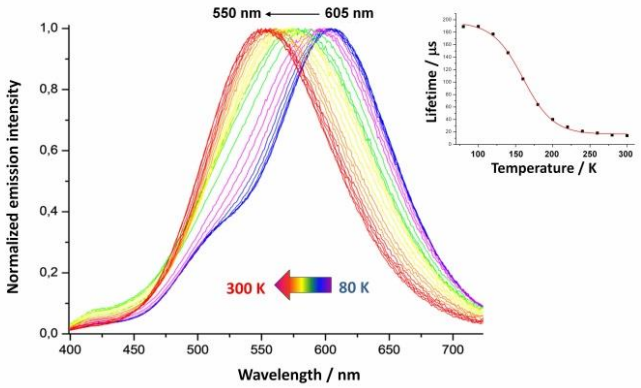

Figure 2. Normalized solid-state temperature dependant emission spectra of $\mathbf{B_c}$ (λ_{ex} = 365 nm); insert: plot of the emission decay lifetime against temperature (80 K to 300 K, the wavelength monitored was the wavelength for which the maximum of signal intensity was observed at a given temperature in the solid-state emission spectra), the red line represents the fit according to the TADF Boltzmann-type equation S1.

$[Cu_2(\mu_2\text{-dppm})_2]^{2+}$ sub-units ($d(Cu^I\text{-}Cu^I)$ = 3.046(2) Å) are significantly shorter than in $\mathbf{B_o}$ (ca. 3.40 Å). Polycrystalline batch of phase $\mathbf{B_c}$ display solid-state luminescence properties that are markedly different from those of the phase $\mathbf{B_o}$.[15] Indeed, derivative $\mathbf{B_c}$ displays in the solid-state at 298 K an intense eye-perceived yellow luminescence under excitation at 365 nm characterized by a broad and featureless band in the emission spectrum with a maximum in intensity at 550 nm (Figure 2), an emissive lifetime τ of 15 µs and a EQY of 42 % (Table 1). Therefore, the species $\mathbf{B_c}$ present a significant red-shift of its emission band and a remarkable increase of its RT EQY ($\mathbf{B_c}$: 42 %; $\mathbf{B_o}$: 2 %) compared to its conformational isomer $\mathbf{B_o}$. Upon cooling from 298 K to 80 K under excitation at 365 nm, emission spectra of derivatives $\mathbf{B_c}$ exhibit gradual red-shifts associated with intense solid state red-orange luminescence at low temperature (Figure 2). At 80 K, the emission spectrum presents a broad and featureless band having an intensity maximum at λ_{em} = 605 nm ($\Delta\lambda_{em(298K/80K)}$ = 0.205 eV / 1653 cm^{-1}), with a shoulder observed at ca. 520 nm, while the emissive lifetime τ increases up to 189 µs. The detailed study of the temperature dependence of the emission lifetime of $\mathbf{B_c}$ (Figure 2) reveals mono-exponential decay times all along the temperature range with a sigmoidal progression that resembles those typically reported for Cu(I) TADF derivatives. In order to account the photophysics observed for the species $\mathbf{B_c}$, it is quite likely that a single radiative relaxation pathway such as a TADF process would be operant along the entire temperature window. Yet, considering the thermal dependence of the emission spectra, the shoulder observed at ca. 520 nm beside the main large emission band centered at ca. 605 nm could suggests that several radiative relaxation pathways operate at low temperature. While this assumption cannot be formally excluded, it is more likely that this shoulder at 520 nm reveals the presence of traces of the $\mathbf{B_o}$ phase or eventually of the $\mathbf{B_g}$ phase (vide supra) in the batch of $\mathbf{B_c}$ crystals manually collected that would have been generated during the process of recovering of the single-crystals of $\mathbf{B_c}$. Therefore, regarding this set of experimental data, a precise and definitive assignment of the relaxation processes occurring after UV-vis excitation in derivative $\mathbf{B_c}$ cannot be provided. Yet, by making the approximation that a TADF process dominates the photophysical processes in the species $\mathbf{B_c}$, a fit of the thermal variation of the τ values of $\mathbf{B_c}$ (Figure 2) to the Boltzmann-type equation S1 in SI derived from the TADF model,[8h,g] was attempted, affording the values of $\Delta E(S_1\text{-}T_1)$ = 767 cm^{-1}, $\tau(S_1)$ = 76 ns and $\tau(T_1)$ = 191 µs. This set of values ranges among those determined for the other Cu^I assemblies based on the $[Cu_2(\mu_2\text{-dppm})_2]^{2+}$ fragment (including the precursor **A**) that were identified as TADF luminophores[9t, 15, 16] which supports the assumption that such relaxation process can be taken into consideration in order to explain the photophysics of the species $\mathbf{B_c}$. Accordingly, the RT k_r radiative rate constant value for $\mathbf{B_c}$ ($2.8*10^4$ s^{-1}, Table 1) is in agreement with a thermally delayed fluorescence regime. Interestingly, in the case of $\mathbf{B_o}$, the RT k_r radiative rate constant value ($1.6*10^3$ s^{-1}, Table 1) supports a ^{3}MLCT phosphorescence rather than a TADF process.[8h,g] This underlines the crucial impact that the structural differences observed between the two confomers $\mathbf{B_o}$ and $\mathbf{B_c}$ have on their photophysical properties, in particular in the radiative relaxation processes. Indeed, while the k_r value for $\mathbf{B_c}$ is one order of magnitude larger than for $\mathbf{B_o}$, the k_{nr} non-radiative rate constant values for both species (Table 1) are significantly similar. This allows assigning the enhancement of the luminescence efficiency of the phase $\mathbf{B_c}$ to more efficient radiative relaxation pathways rather than reduced vibrational non-radiative processes lying at RT in $\mathbf{B_c}$'s scaffold compared to $\mathbf{B_o}$. Likely, the significant decrease of the intermetallic $Cu^I\text{-}Cu^I$ distances in the $[Cu_2(\mu_2\text{-dppm})_2]$ sub-units of $\mathbf{B_c}$ is a parameter that plays a role, at least partially, for such differences. It can induce an increase of the SOC components in the different processes, which favors radiative relaxation processes in particular when compared with the conformer $Cu^I_8Pd^{II}_1$ in $\mathbf{B_o}$.

Regarding the remarkable differences recorded in the solid-state luminescence properties between the weakly luminescent conformer $\mathbf{B_o}$ and the bright luminescent conformer $\mathbf{B_c}$, we have triggered quantum chemical DFT molecular calculations to give insights into the reasons why the less emissive species $\mathbf{B_o}$ is predominantly obtained in the crystallization experiments.[19] The energies of the $\mathbf{B_o}$ and $\mathbf{B_c}$ $Cu^I_8Pd^{II}_1$ molecular conformers were calculated by freezing the copper atomic positions in their crystallographic configurations. Full geometry optimization was also performed. It revealed firstly that the energy difference in vacuum between the $\mathbf{B_o}$ and $\mathbf{B_c}$ $Cu^I_8Pd^{II}_1$ conformers is small (ΔE = 14.6 kJ mol^{-1}). Quite unexpectedly at first sight regarding experimental results, the $Cu^I_8Pd^{II}_1$ in $\mathbf{B_o}$ is the less stable conformer (Figure 3a). Additionnaly, the most stable calculated conformer in vacuum ($\mathbf{B_{calc}}$) is notably different from the experimental isomers found in $\mathbf{B_o}$ and $\mathbf{B_c}$ (Figure 3a). $\mathbf{B_{calc}}$ is based on an almost planar $Cu_8Pd_1(CN)_8$ core bearing two internal μ_2-CN and two internal μ_3-CN ligands (Figure 3b). Interestingly, while the calculated species $\mathbf{B_{calc}}$ is less symmetrical than the experimentally observed conformers $\mathbf{B_o}$ and $\mathbf{B_c}$, it bears 'intermediate' geometrical features with two sets of different intermetallic $Cu^I\text{-}Cu^I$ distances in the $[Cu_2(\mu_2\text{-dppm})_2]$ sub-units (Table 1), associated either with μ_3-CN internal ligands (2.920 Å) or μ_2-CN internal ligands (3.128 Å). Apart from these intermetallic distances and the bridging coordination mode of the internal cyanido ligands, all the gross geometrical parameters are essentially similar within the series of the $\mathbf{B_{calc}}$, $\mathbf{B_o}$ and $\mathbf{B_c}$ conformers. The calculated isomer $\mathbf{B_{calc}}$ can be considered as a molecular scaffold, in vacuum, in which is optimized the balance of energetic stabilization and destabilization factors that are

Table 1. Intermetallic Cu^{I}-Cu^{I} distances in the $[Cu_2(\mu_2\text{-dppm})_2]$ fragments at 150 K, photophysical data for species $\mathbf{B_o}$ (λ_{ex} = 350 nm), $\mathbf{B_c}$ (λ_{ex} = 365 nm), $\mathbf{B_g}$ (λ_{ex} = 375 nm) and $\mathbf{B_m}$ (λ_{ex} = 375 nm) at 298 K in the solid-state and calculated data for $\mathbf{B_{cal}}$.

	d(Cu-Cu) (Å)	λ_{em} (nm)[a]	Φ_{em}	τ_{obs} (µs)[a]	k_r (s^{-1})[b]	k_{nr} (s^{-1})[c]
$\mathbf{B_o}$[15]	3.362(1) 3.408(1) 3.453(1) 3.459(1)	500 (515)	2	12 (222)	$1.6*10^3$	$8.2*10^4$
$\mathbf{B_c}$	3.046(2)	550 (605)	42	15 (189)	$2.8*10^4$	$3.9*10^4$
$\mathbf{B_{cal}}$[d]	2.920 3.128	[535]$_I$[d]	-	-	-	-
$\mathbf{B_g}$	-	500 (520)	27	39 (282)	$6.3*10^3$	$1.7*10^4$
$\mathbf{B_m}$	-	559 (538)	7	35 (248)	$2.0*10^3$	$2.6*10^4$

[a] Data recorded at 80 K are given in parentheses; [b] $k_r = \Phi_{em}/\tau_{obs}$; [c] $k_{nr} = (1-\Phi_{em})/\tau_{obs}$; [d] Calculated molecular structure and calculated phosphorescence wavelength at 0 K given in brackets.

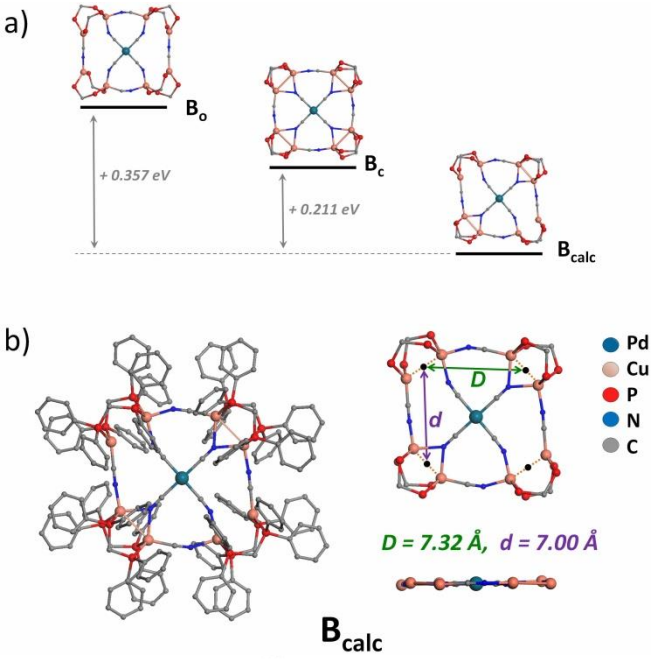

Figure 3. a) Relative energies in vacuum of the species $\mathbf{B_o}$, $\mathbf{B_c}$ and $\mathbf{B_{calc}}$ (phenyl rings and protons have been removed for the sake of clarity); b) View of the calculated molecular structure of $\mathbf{B_{calc}}$ (protons have been removed for clarity), simplified 'top' and side views of the species $\mathbf{B_{calc}}$.

mainly the steric constraints (intramolecular repulsion between the phenyl rings of the dppm ligand belonging to different $[Cu_2(\mu_2\text{-dppm})_2]$ fragments) and stabilizing interactions (metallophilic interactions in the Cu^{I} dimers resulting of short Cu^{I}-Cu^{I} distances, coordination modes of the cyanido ligands…). Considering the overall moderate energy differences between $\mathbf{B_{calc}}$, $\mathbf{B_o}$ and $\mathbf{B_c}$, (Figure 3a), multiple and complex fast equilibria based on intramolecular exchanges requiring minimum reorganization (mostly translation/rotation of the CN groups) must occur in solution at RT, allowing easy interconversion between these conformers. This allows concluding that all the three conformers and other intermediate structures must be present in solution at RT, an almost barrierless geometry reorganizations connecting the different arrangements. It can be deduced that it is the crystal growth which induces the predominance of isomer $\mathbf{B_o}$ at the solid-state. Such a selection in the solid state of the less stable of the two experimentally determined conformers can be assigned to the fact that the $Cu^{I}_8Pd^{II}_1$ assemblies $\mathbf{B_o}$ stacks on the top of each other in the crystalline solid state along infinite columns (Figure 1a) in which multiple lateral stabilizing CH-π non-covalent interactions are cumulated between most of the phenyl rings of the dppm ligands of neighboring assemblies. In a marked contrast, in the crystalline solid state, the $Cu^{I}_8Pd^{II}_1$ species in $\mathbf{B_c}$ appear much more isolated from each other (Figure 1b), bearing less peripheral non-covalent CH-π interactions. This may explain why this conformer is only observed as traces along crystallization experiments. Finally, the lower symmetry observed in the molecular scaffold $\mathbf{B_{calc}}$ probably does not promote the formation, in the crystalline solid-state, of a set of cumulated stabilizing non-covalent intermolecular interactions as large as those experimentally observed in the case of the conformers $\mathbf{B_o}$ and $\mathbf{B_c}$, which likely preclude its formation as single crystal. Therefore, the accumulation of stabilizing CH-π non-covalent interactions along the crystallization process allows an inversion in the hierarchy observed in vacuum considering the relative stabilities of the conformers $\mathbf{B_{calc}}$, $\mathbf{B_o}$ and $\mathbf{B_c}$. This dictates the almost exclusive isolation in fine of the species $\mathbf{B_o}$. This behavior definitively favored by the very labile, flexible and low-directional coordination sphere of the Cu^{I} ions that can accept manifold changes in their coordination numbers, bond lengths and angles for the expense of a minimal energy cost. This situation carries also a great impact on the electronic structures of these species as witnessed by the remarkable differences observed in the solid-state concerning the photophysical behaviors of conformers $\mathbf{B_o}$ and $\mathbf{B_c}$ (Table 1).

Regarding the molecular scaffold calculated for the more stable specie (in vacuum) $\mathbf{B_{calc}}$ which carry a set of geometrical parameters significantly different than those observed experimentally in $\mathbf{B_o}$, it can be anticipated that the photophysical processes lying in the $\mathbf{B_{calc}}$ scaffold should be markedly different compared to those observed for $\mathbf{B_o}$, affording putatively an attractive new luminescent phase. This has triggered us to study the mechanochromic response of solid-state polycrystalline samples of $\mathbf{B_o}$, anticipating that a partial amorphization or alteration of the pristine crystalline state organization would occur upon grinding. This would impact the long range columnar stacks observed in single crystals of $\mathbf{B_o}$ (Figure 1a) allowing some $Cu^{I}_8Pd^{II}_1$ assemblies to relax to an energetically more favored conformer bearing a molecular structure related to the one calculated in $\mathbf{B_{calc}}$, and therefore alterating the photophysical characteristics of the bulk solid. Indeed, a manual grinding at RT of the polycrystalline powder of $\mathbf{B_o}$, affords the $\mathbf{B_g}$ phase (Scheme 1). The very weak greenish emission typical of $\mathbf{B_o}$[15] under UV-vis lamp light excitation (λ_{ex} = 365 nm) is transferred to a much brighter eye-perceived yellow-green emission, revealing a naked-eye highly observable mechanochromic effect.[20] Concomitantly, no alteration of the white color initially

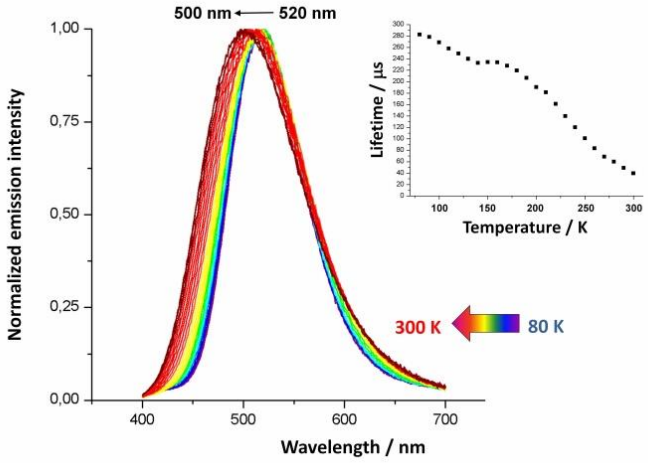

Figure 4. Normalized solid-state temperature dependant emission spectra of $\mathbf{B_g}$ (λ_{ex} = 375 nm); insert: plot of the emission decay lifetime against temperature (80 K to 300 K, the wavelength monitored was the wavelength for which the maximum of signal intensity was observed at a given temperature in the solid-state emission spectra).

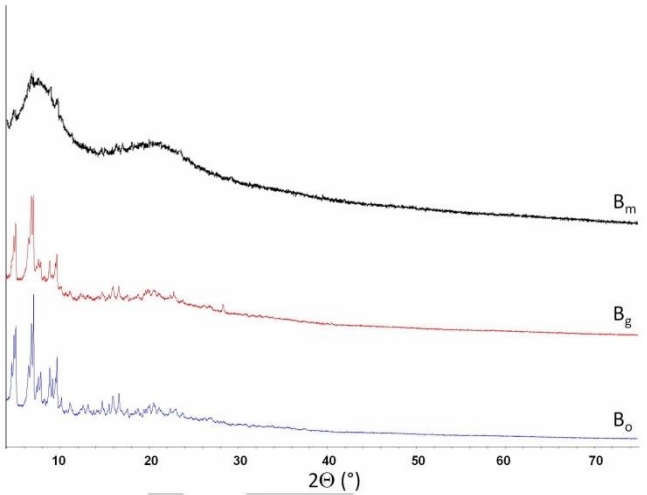

Figure 5. PXRD patterns of a) $\mathbf{B_o}$, b) $\mathbf{B_g}$ and c) $\mathbf{B_m}$ angles.

presented under visible light by the solid-state sample of $\mathbf{B_o}$ is observed during the grinding process. The RT emission of the $\mathbf{B_g}$ phase correspond to a large band centered at 500 nm (Figure 4, λ_{ex} = 375 nm), revealing no spectral shift compared to the RT emission of $\mathbf{B_o}$. The emissive lifetime τ is 39 µs at 298 K. Importantly, a remarkable change in the intensity of the luminescence signal is observed with an increase of the EQY from 2 % for $\mathbf{B_o}$ to reach 27% for $\mathbf{B_g}$ (Table 1). The RT photoluminance (measured with a flux of 3.55 W/m² for an excitation at 365 nm) of the solid-state samples of $\mathbf{B_g}$ (16.56 Cd/m²) is also significantly higher than for $\mathbf{B_o}$ (0.832 Cd/m²). Upon cooling from 290 K to 80 K under excitation at 375 nm, emission spectrum of derivative $\mathbf{B_g}$ exhibits a gradual red-shift associated with intense solid state yellowish luminescence at low temperature (Figure 4). Thus, at 80 K, the profile of the emission spectrum presents a broad featureless band having an intensity maximum at λ_{em} = 522 nm, revealing a slightly larger red-shift at low temperature for $\mathbf{B_g}$ than for $\mathbf{B_o}$ (λ_{em} = 515 nm at 80 K). The average emissive lifetime τ at 80 K increases up to 282 µs which is larger, but kept in the same range of values, than for $\mathbf{B_o}$ (222 µs) and for $\mathbf{B_c}$ (189 µs). The temperature dependence of the emission lifetime of $\mathbf{B_g}$ (Figure 4) was analyzed considering mono-exponential decay times all along the temperature range. It revealed an irregular but reproducible profile progression[20] upon cooling with a constant increase of the decay time value of the exited state (Figure 4). It is quite common that multiple emissions are detected in samples obtained after grinding treatments arising from multiple species and site heterogeneity.[9p,12] Regarding the variety of possible conformers (not only limited to $\mathbf{B_o}$, $\mathbf{B_c}$ and $\mathbf{B_{calc}}$, since the quantum chemical DFT calculations performed do not consider intermolecular non-covalent interactions that may have crucial importance in the selection in the solid-state of a specific conformer) ranged in a quite narrow distribution of relative energies, it is not surprising that a grinding process applied on a polycrystalline sample of $\mathbf{B_o}$ would indeed afford several different emissive species based on structurally related polymetallic scaffolds. Therefore, the irregular profile[20] of the thermal dependence of the average decay time of the excited state recorded for $\mathbf{B_g}$ samples may account for cumulated independent contributions assigned to different emissive centers whose ratios are not clearly determinated. This precludes performing a deeper analysis of the set of data obtained for the thermal dependence of the observed decay time based on a treatment of the experimental data considering multi-exponential decay times. Yet, the value of the RT observed k_r radiative rate constant that can be extracted for these measurements (Table 1) suggests that phosphorescence processes dominate at RT.

PXRD studies were conducted on $\mathbf{B_g}$ samples to get insights about the structural modifications potentially induced by the application of the mechanical stress on $\mathbf{B_o}$.[21] The diagram recorded for $\mathbf{B_g}$ reveals a set of peaks that compares well with those observed in the diagram obtained for polycrystalline samples of $\mathbf{B_o}$ (Figure 5). This suggests that neither a complete amorphization nor crystal phase transitions take place during the application of the manual grinding on solid-state samples $\mathbf{B_o}$. A mechanically induced chemical transformation is also precluded since $\mathbf{B_g}$ phase dissolved in CD_2Cl_2 afforded similar multinuclear NMR spectra[19] than those recorded for $\mathbf{B_o}$[15] and afforded single crystals of $\mathbf{B_o}$ when recrystallized from CH_2Cl_2 upon pentane vapors diffusion. Yet, the peaks observed in the diagram of $\mathbf{B_g}$ are significantly broader and less intense than for $\mathbf{B_o}$ which supports the assumption of a partial amorphization of the bulk sample. Likely, the grinding process induces local effects, allowing the formation of new emissive species in low amount. This phenomenon was previously reported by Perruchas *et al.* investigating the mechanochromic behavior of Cu_4I_4 cubane clusters stabilized by phosphane ligands.[12] It was assigned to an effect of the mechanical stress application on the crystallite sizes and/or generation of microstrains which induces local apparition in a bulk composite sample of a small amount of a new generated amorphous emissive domains in addition to the original pristine crystalline phase. SEM pictures (Figure 6) recorded for $\mathbf{B_o}$ and $\mathbf{B_g}$ support this assumption since significantly similar patterns were observed in both cases revealing polycrystalline particles having quite a large size distribution with smaller average dimensions for $\mathbf{B_g}$ samples likely as a result of the grinding process. Therefore, in accordance with previously reported related manual grinding processes applied on Cu_4I_4 cubane clusters,[12a] an incomplete

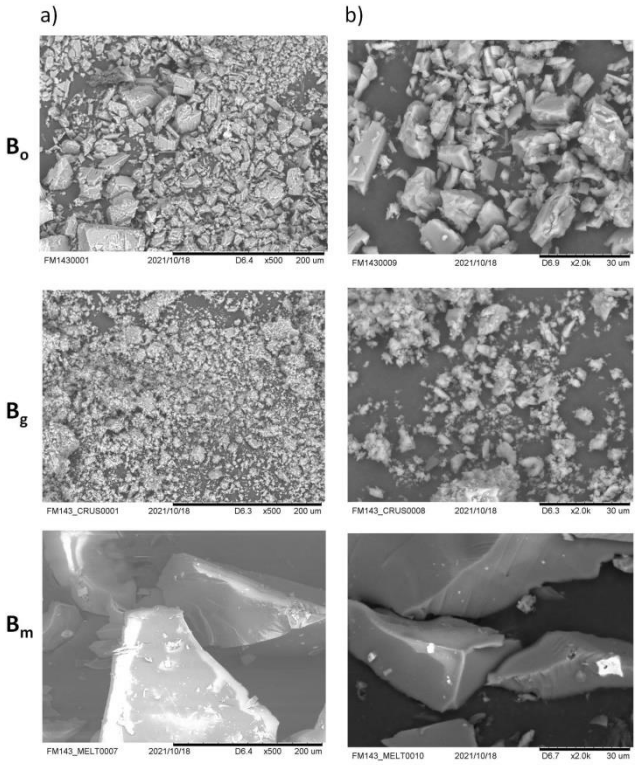

Figure 6. SEM images of $\mathbf{B_o}$, $\mathbf{B_g}$ and $\mathbf{B_m}$ samples taken for a) 500 magnification and b) 2000 magnification.

transformation of the crystalline state observed in the $\mathbf{B_o}$ phase likely occurs upon application of a mechanical stress, affording a new $\mathbf{B_g}$ phase with altered bulk luminescence properties. Interestingly, the TGA-DSC analysis of $\mathbf{B_o}$ showed an endothermic peak around 230 °C associated with no loss of mass, while the thermal decomposition started to occur at ca. 300 °C.[19] The peak at 230 °C corresponds to a melting transition and no exothermic peak is observed upon cooling the sample back to RT before the decomposition temperature was reached, probing that a recrystallization process does not occur. Accordingly, the visible appearance of bulk samples of polycrystalline white powder of $\mathbf{B_o}$ after being heated at 240°C and cooled back to RT changed to colorless clear glass-like solids, affording the new phase $\mathbf{B_m}$ (Scheme 1). Under UV-vis lamp light excitation (λ_{ex} = 365 nm) at RT, samples of $\mathbf{B_m}$ exhibited an eye-perceived yellowish emission, clearly different from the very weak greenish emission of $\mathbf{B_o}$.[15] The PXRD diagram of $\mathbf{B_m}$ showed two broad peaks around 8° and 20°, revealing an amorphous phase that is markedly different from the $\mathbf{B_o}$ and $\mathbf{B_g}$ phase.[21] Therefore, the melting process implies a considerably larger solid-state organization alteration than the manual mechanical grinding process. Supporting this observation, SEM pictures taken for $\mathbf{B_m}$ sample (Figure 6) revealed particles with larger average size than those observed for $\mathbf{B_o}$ and $\mathbf{B_g}$, with a flat and homogeneous surface microstructure suggesting that the melting process yielded a vitreous phase, in agreement with the PXRD diagram of $\mathbf{B_m}$.

The RT solid-state emission spectrum of the $\mathbf{B_m}$ presents a large featureless band centered at 559 nm (Figure 7, λ_{ex} = 375 nm), which is significantly red shifted compared to the RT emission of $\mathbf{B_o}$ and $\mathbf{B_g}$ (ca. 500 nm) but comparable with the emission spectrum of $\mathbf{B_c}$ (550 nm). The emissive lifetime τ is 35 μs at 298 K. The RT EQY is 7 % and the RT photoluminance reaches (4.24 Cd/m², measured with flux of 3.55 W/m² for an excitation at 365 nm) values that are both ranging between those measured for $\mathbf{B_o}$ and $\mathbf{B_g}$.

Temperature dependent solid-state measurements of the emission spectra and the decay time of the excited state of $\mathbf{B_m}$ were conducted. Upon cooling from 298 K to 80 K under excitation at 375 nm, emission spectra of derivative $\mathbf{B_m}$ exhibit gradual blue-shifts associated with a solid-state eye-perceived greenish luminescence at low temperature (Figure 7). The emission spectrum at 80 K presents a broad featureless band having an intensity maximum at λ_{em} = 538 nm. Such a hypsochromic shift upon cooling does not follow the trend observed for the phases $\mathbf{B_o}$,[15] $\mathbf{B_c}$ and $\mathbf{B_g}$ in which a gradual red-shift upon cooling is observed (Figure 2 and 4). This confirms the large impact on the photophysical properties of the $Cu^{I}_{8}Pd^{II}_{1}$ assembly of the various large-scale organizations that can be encountered in the solid-state for this polymetallic assembly. Thermally induced chemical reaction in the solid-state that would have altered the initial chemical structure of this metallacyclic assembly is precluded since dissolution in CD_2Cl_2 of the $\mathbf{B_m}$ phase afforded $^{31}P\{^{1}H\}$ and ^{1}H NMR spectra similar to those recorded for dissolved $\mathbf{B_o}$ and $\mathbf{B_g}$ phases.[19] In addition, recrystallization of the $\mathbf{B_m}$ phase from CH_2Cl_2 solution exposed to pentane vapors afforded single crystals of the $\mathbf{B_o}$ species in high yield. The thermal dependence of the emission decay time of the species $\mathbf{B_m}$ was treated successfully considering mono-exponential decay times all along the temperature range, revealing a sigmoidal profile with a smooth and constant progression upon temperature cooling from 35 μs at 298 K to 248 μs at 80 K. Considering this set of data, it is possible to state that the temperature dependences of the photophysical properties in $\mathbf{B_m}$ are suggestive of the absence of a TADF mechanism. The hypsochromic shift upon cooling of emission maxima upon temperature variation is indeed not consistent with such a photophysical process. In addition, the value of the RT k_r radiative rate constant (Table 1) supports a ^{3}MLCT phosphorescence process to account for the radiative processes observed at room temperature. The blue shift observed at low temperature for the emission maxima is in agreement with the rigidochromic effect that results from the increased rigidity at low temperature, leading to a smaller excited state distortion. In addition, a narrowing of the emission band width with decreasing temperature is also observed, in line with the lower accessibility of higher vibrational states at low temperature. The impact of the non-covalent intermolecular interactions in the various solid-state arrangements displayed by the different phases obtained for the $Cu^{I}_{8}Pd^{II}_{1}$ assembly is also essential at the excited state as it is highlighted by the difference of photoluminescence properties between the $\mathbf{B_o}$ and $\mathbf{B_c}$ phases.

On the computational point of view, the optimization of the full solid-state structures at the excited states of these phases taking into account these non-covalent intermolecular interactions would be necessary to explain these differences, calculations which are not accessible to date. The observed partial or full amorphization of $\mathbf{B_o}$ and $\mathbf{B_g}$ phases is consistent with a release of the intermolecular interactions. In that case, full geometry optimizations based on the TD-DFT gradients of first singlet (S_1) and triplet (T_1) excited states of the $Cu^{I}_{8}Pd^{II}_{1}$ assembly could give substantial information to understand the photophysics observed.[19] This allows to access to the

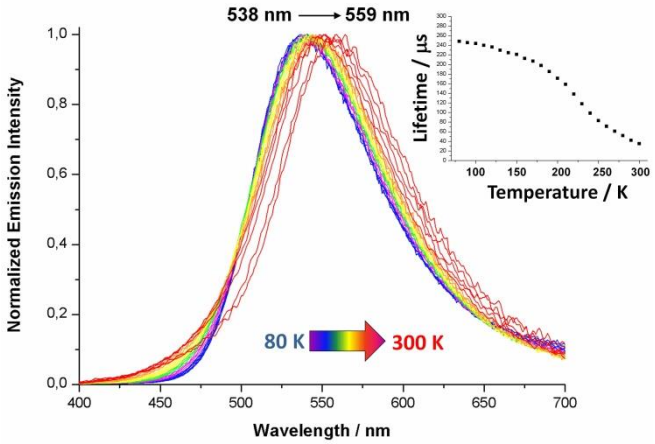

Figure 7. Normalized solid-state temperature dependant emission spectra of $\mathbf{B_m}$ (λ_{ex} = 375 nm); insert: plot of the emission decay lifetime against temperature (80 K to 300 K, the wavelength monitored was the wavelength for which the maximum of signal intensity was observed at a given temperature in the solid-state emission spectra).

geometries of these excited states in vacuum or more generally in a non-constraining intermolecular environment. The resulting calculated geometries are sketched in Figure 8a. Interestingly, whereas $\mathbf{B_{calc}}$ was the starting geometry (Figure 3) used to conduct these full geometry optimizations, the relaxation of the excited states $\mathbf{S_{1\text{-}relax}}$ and $\mathbf{T_{1\text{-}relax}}$ leads to arrangements having molecular organizations (Figure 8) being in the first glimpse similar to $\mathbf{B_o}$ (Figure 1) on the bonding point of view. Yet, the intermetallic Cu(I)-Cu(I) distances in the $[Cu_2(\mu_2\text{-dppm})_2]^{2+}$ fragments present a larger distribution in these relaxed excited states' geometries (intermetallic distance distribution : $\mathbf{B_o}$, 3.362 – 3.459 Å ; $\mathbf{S_{1\text{-}relax}}$, 3.272– 3.634 Å ; $\mathbf{T_{1\text{-}relax}}$, 3.362– 3.546 Å) and larger D and d distances (Figures 3 and 8) measured in the '$Pd_1Cu_8CN_8$' cyclic organic cores. Moreover as revealed by the comparison displayed in the figure 8b, the '$Pd_1Cu_8CN_8$' cyclic organic cores in the $\mathbf{S_{1\text{-}relax}}$ and $\mathbf{T_{1\text{-}relax}}$ are significantly more distorted from a strictly planar organization than in the case of the $\mathbf{B_o}$ scaffold (maximum deviation from the mean plane : $\mathbf{B_o}$, 0.66 Å ; $\mathbf{S_{1\text{-}relax}}$, 0.85 Å ; $\mathbf{T_{1\text{-}relax}}$, 0.79 Å). Therefore, all in all, the geometries of the relaxed excited states $\mathbf{S_{1\text{-}relax}}$ and $\mathbf{T_{1\text{-}relax}}$ are less planar and more distorted than the scaffold observed in the $\mathbf{B_o}$ phase. In addition, as compared to the $\mathbf{B_{calc}}$ arrangement (Figure 3 and Table 1), a significant elongation of the average intermetallic distances in the $[Cu_2(\mu_2\text{-dppm})_2]^{2+}$ fragments is observed (+0.46 Å for $\mathbf{S_{1\text{-}relax}}$ and +0.42 Å for $\mathbf{T_{1\text{-}relax}}$) but in each of the two relaxed excited state one of the four bimetallic subunits is significantly more affected than the three others with a Cu^I-Cu^I distance of 3.634 Å for $\mathbf{S_{1\text{-}relax}}$ and 3.546 Å for $\mathbf{T_{1\text{-}relax}}$. The nature of the excited state $\mathbf{T_{1\text{-}relax}}$ radiative relaxation is better described as a metal-ligand to ligand excitation as revealed by the difference density map shown in Figure 8c. The associated emission wavelength arising from this excited state is calculated at 535 nm which is in line with the experimental observation at low temperature for the fully amorphous phase $\mathbf{B_m}$ (538 nm, Table 1) which a priori correspond to the phase where the long range organization due to extended network of intermolecular interactions has been very likely mostly vanished. The difference in energy between the relaxed $\mathbf{S_{1\text{-}relax}}$ and $\mathbf{T_{1\text{-}relax}}$ arrangements is of 2090 cm^{-1}, a value hardly compatible with TADF process and supports the assignment of the experimental photophysical measurements to a ^{3}MLCT phosphorescence process for the fully amorphous phase $\mathbf{B_m}$. It is yet important to

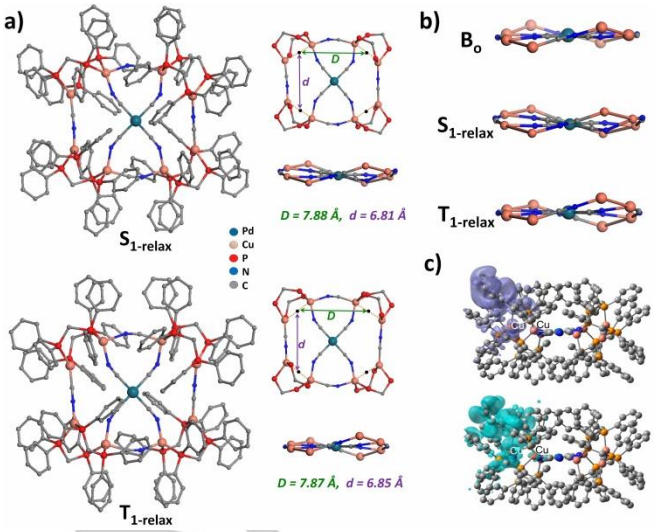

Figure 8. a) General geometries, simplified 'top' and 'side' views of the optimized geometries of $\mathbf{S_{1\text{-}relax}}$ (top) and $\mathbf{T_{1\text{-}relax}}$ (bottom), (H atoms omitted), b) comparative side simplified 'side' views of the experimental molecular structure of $\mathbf{B_o}$ and of the of the optimized geometries of $\mathbf{S_{1\text{-}relax}}$ and $\mathbf{T_{1\text{-}relax}}$, c) Iso-surface representations of the electronic charge-density difference between the $\mathbf{T_1}$ excited state and the density of the closed shell singlet at this geometry ($\mathbf{S_0}^{\#}$): green = density depletion; purple = density increase; the iso-surface is ±1.10^{-4} e/bohr^3.

stress that these relaxed excited states in vacuum correspond to isolated molecules and cannot strictly reproduce the situation encountered experimentally in the different $Cu^I_8Pd^{II}_1$ assemblies' phases in their solid-state environment in which weak intermolecular interactions should occur locally between the discrete molecules. Therefore, in spite of the good agreement between the calculated values and the experimental photophysics measured for $\mathbf{B_m}$ in particular, these results are mostly indicative and do not allow unambiguous assignation of the photophysics observed in the non-crystalline phase $\mathbf{B_m}$.

As previously discussed, the selection of the $\mathbf{B_o}$ geometry is very likely favored by the formation in the crystalline solid-state of one dimensional infinite columnar stacks that propagate perpendicular to the mean planes of the $Cu^I_8Pd^{II}_1$ assemblies. Due to such organisation in the $\mathbf{B_o}$ phase, distortion of the molecular scaffolds in the excited states in this phase as observed in $\mathbf{S_{1\text{-}relax}}$ and $\mathbf{T_{1\text{-}relax}}$ geometries is very probably energetically disfavored since it should induce a long-range re-organisation of the intermolecular interactions between the $Cu^I_8Pd^{II}_1$ assemblies. This might explain the differences in the photophysical properties observed experimentally in the $\mathbf{B_o}$ and $\mathbf{B_m}$ phases and those anticipated from the calculated relaxed excited states in vacuum, in spite of the gross geometrical similarities of the $Cu^I_8Pd^{II}_1$ assemblies in $\mathbf{B_o}$, $\mathbf{S_{1\text{-}relax}}$ and $\mathbf{T_{1\text{-}relax}}$. Finally, it is interesting to note that the $Pd(CN)_4$ moieties within the calculated arrangements are almost unchanged upon excitation and are also similar to the $\mathbf{B_o}$ and $\mathbf{B_c}$ experimental molecular structures. While these square planar fragments do play an important role as structuring group, they do not contribute directly to the photophysical properties' differences between the different phases, allowing to assign the stimuli sensitive properties observed to the specificities of the

coordination chemistry and electronic configurations of the Cu(I)-based sub-units.

Conclusion

With the characterization of the minor crystalline phase $\mathbf{B_c}$ in addition to the previously observed $\mathbf{B_o}$ species, the variety of the molecular geometries that can be observed in the $Cu^{I}_{8}Pd^{II}_{1}$ multimetallic assembly is highlighted, as well as the major impact of these geometries on the photophysical properties of solid-state samples of the $Cu^{I}_{8}Pd^{II}_{1}$ derivative. DFT calculations highlight that a third conformer $\mathbf{B_{calc}}$ presents the optimized geometry in vacuum, which allows concluding that the selection of the $\mathbf{B_o}$ species in the solid-state is due to cumulated intermolecular non-covalent π-CH interactions within columnar stacks. Importantly, the diversity of the molecular scaffold that can be encountered in the solid-state for the $Cu^{I}_{8}Pd^{II}_{1}$ assembly is associated with overall moderate energy differences between all possible conformers. Easy interconversions between these conformers explain the large predominance of the $\mathbf{B_o}$ species as the $Cu^{I}_{8}Pd^{II}_{1}$ assembly derivative is recrystallized from the solution. The labile, flexible and low-directional coordination sphere of the Cu^{I} ions that can accept manifold geometry changes at the expense of a minimal energy cost definitively favors such behaviors. More importantly, these interconversions between possible conformers can be also manipulated in the solid-state by applying mechanical and thermal stress to pristine solid-state samples of $\mathbf{B_o}$, affording respectively new luminescent species $\mathbf{B_g}$ and $\mathbf{B_m}$. The analysis of the various photophysical properties of this set of phases obtained for $Cu^{I}_{8}Pd^{II}_{1}$ assembly suggests that such stress-induced conformers conversions govern a subtle balance between different ^{3}MLCT phosphorescence ($\mathbf{B_o}$, $\mathbf{B_g}$ and $\mathbf{B_m}$ phases) and TADF ($\mathbf{B_c}$ phase) relaxation processes. Therefore, playing with the non-covalent intermolecular interactions between individual molecular species allows tailoring the conformer scaffold present in the solid-state, giving an access to markedly different solid-state emitters generated from the same chemical structure.

It is here important to stress that, while the $\mathbf{B_o}$ phase almost exclusively collected in the solid-state after the synthetic work-up is conducted is a weak RT luminophore, it allows to obtain the much more RT emissive material $\mathbf{B_g}$ after grinding. Indeed the EQY and photoluminance values are approximatively fifteen times larger for $\mathbf{B_g}$ than for $\mathbf{B_o}$. This result highlights that the solid-state studies of the photophysics of Cu(I) based derivatives should not been restricted to the crystalline samples from which new highly luminescent phases can be obtained from thermal or mechanical treatments. Such stimuli-responsive behavior, that is likely to be promoted with luminescent coordination-driven Cu(I) polymetallic assemblies, offers therefore promising perspectives for this class of derivatives in the field of the design and study of stimuli-sensitive photoactive materials, but also for the preparation of new innovative emittors for lighting applications.

Acknowledgements

This work was supported by the CNRS, the ANR (ANR PRC SMAC and ANR PRCI SUPRALUM), the French 'Ministère de l'Enseignement supérieur, de la Recherche et de l'Innovation' and the French 'Ministère des Affaires Etrangères'. C.L. thanks the Alexander von Humboldt Foundation for a fellowship for experienced researcher. K.C. and V.D. acknowledges support by the "Grand équipement national de calcul intensif (GENCI)" through HPC resources of CINES, TGCC and IDRIS (grants 2020/2021-A0080800649/A0100800649).

Keywords: polymetallic Cu(I) ion complexes • conformers • luminescence • mechanochromism • TD DFT calculations

[1] a) B. Minaev, G. Baryshnikov, H. Agren, *Phys. Chem. Chem. Phys.* **2014**, *16*, 1719-1758; b) Z. Liu, M. F. Qayyum, C. Wu, M. T. Whited, P. I Djurovich, K. O. Hodgson, B. Hedman, E. I. Solomon, M. E. Thompson, *J. Am. Chem. Soc.* **2011**, *133*, 3700-3703; c) A. Salehi, X. Fu, D.-H. Shin, F. So, *Adv. Funct. Mater.* **2019**, *29*, 1808803; d) M. Y. Wong, E. Zysman-Colman, *Adv. Mater.* **2017**, *29*, 1605444; e) A. K.-W. Chan, M. Ng, Y.-C. Wong, M.-Y. Chan, W.-T. Wong, V. W.-W. Yam, *J. Am. Chem. Soc.* **2017**, *139*, 10750-10761; f) Z.-Q. Zhu, C.-D. Park, K. Klimes, J. Li, *Adv. Opt. Mater.* **2019**, *7*, 1801518.

[2] O. S. Wenger, *Nat. Chem.* **2020**, *12*, 323-324.

[3] a) Y. Sagara, T. Kato, *Nat. Chem.* **2009**, *1*, 605-610; b) K. K.-W. Lo, M.-W. Louie, K. Y. Zhang, *Coord. Chem. Rev.* **2010**, *254*, 2603-2622; c) K. K.-W. Lo, *Acc. Chem. Res.* **2020**, *53*, 32-44; d) D. Yan, D. G. Evans, *Mater. Horiz.* **2014**, *1*, 46-57; e) A. S.-Y. Law, L. C.-C. Lee, K. K.-W. Lo, V. W.-W. Yam, *J. Am. Chem. Soc.* **2021**, *143*, 5396-5405; f) D.-L. Ma, H.-Z. He, K.-H. Leung, D. S.-H. Chan, C.-H. Leung, *Angew. Chem. Int. Ed.* **2013**, *52*, 7666-7682; g) X. He, V. W.-W. Yam, *Coord. Chem. Rev.* **2011**, *255*, 2111-2123; h) V. W.-W. Yam, K. M.-C. Wong, *Chem. Comm.* **2011**, *47*, 11579-11592.

[4] a) O. Guillou, C. Daiguebonne, G. Calvez, K. Bernot, *Acc. Chem. Res.* **2016**, *49*, 844-856; b) W. Liu, Y. Fang, G. Z. Wei, S. J. Teat, K. Xiong, Z. Hu, W. P. Lustig, J. Li, *J. Am. Chem. Soc.* **2015**, *137*, 9400-9408; c) Y. Ma, K. Chen, J. Lu, J. Shen, C. Ma, S. Liu, Q. Zhao, W.6Y. Wong, *Inorg. Chem.* **2021**, *60*, 7510-7518; d) Y. Jiang, G. Li, W. Che, Y. Liu, B. Xu, G. Shan, D. Zhu, Z. Su, M. R. Bryce, *Chem. Comm.* **2017**, *53*, 3022-3025.

[5] a) S. Ito, *Chem. Lett.* **2021**, *50*, 649-660; b) S. Perruchas, *Dalton Trans.* **2021**, *50*, 12031-12044.

[6] a) L. Huang, C. Qian, Z. Ma, *Chem. Eur. J.* **2020**, *26*, 11914-11930; b) M. Yang, I. S. Park, Y. Miyashita, K. Tanaka, T. Yasuda, *Angew. Chem. Int. Ed.* **2020**, *59*, 13955-13961; c) S. Nagai, M. Yamashita, T. Tachikawa, T. Ubukata, M. Asami, *J. Mater. Chem. C* **2019**, *7*, 4988-4998; d) S.-N. Lei, H. Xiao, Y. Zeng, C.-H. Tung, L.-Z. Wu, H. Cong, *Angew. Chem. Int. Ed.* **2020**, *59*, 10059-10065; e) K. Isayama, N. Aizawa, J. Y. Kim, T. Yasuda, *Angew. Chem. Int. Ed.* **2018**, *57*, 11982-11986; f) J. Guan, F. Xu, C. Tian, L. Pu, M.-S. Yuan, J. Wang, *Chem. – Asian J.* **2019**, *14*, 216-222; g) H. Tsujimoto, D.-G. Ha, G. Markopoulos, H. S. Chae, M. A. Baldo, T. M. Swager, *J. Am. Chem. Soc.* **2017**, *139*, 4894-4900; h) Z. Yang, Z. Chi, Z. Mao, Y. Zhang, S. Liu, J. Zhao, M. P. Aldred, Z. Chi, *Mater. Chem. Front*. **2018**, *2*, 861-890.

[7] a) H. Ito, M. Muromoto, S. Kurenuma, S. Ishizaka, N. Kitamura, H. Sato, T. Seki, *Nat. Commun.* **2013**, *4*, 2009-2014; b) J. Schneider, Y.-A Lee, J. Pérez, W. W. Brennessel, C. Flaschenriem, R. Eisenberg, *Inorg. Chem.* **2008**, *47*, 957-968; c) A. Laguna, T. Lasanta, J. M. Lopez-de-Luzuriaga, M. Monge, P. Naumov, M. E. Olmos, *J. Am. Chem. Soc.* **2010**, *132*, 456-457; d) M. Osawa, I. Kawata, S. Igawa, M. Hoshino, T. Fukunaga, D. Hashizume, *Chem. Eur. J.* **2010**, *16*, 12114-12126; e) I. O. Koshevoy, C.-L. Lin, A. J. Karttunen, M. Haukka, C.-W. Shih, P.-T. Chou, S. P. Tunik, T. A. Pakkanen, *Chem. Commun.* **2011**, *47*, 5533-5535; f) A. Deak, C. Jobbagy, G. Marsi, M. Molnar, Z. Szakacs, P. Baranyai, *Chem. Eur. J.* **2015**, *21*, 11495-11508; g) Z. Chen, J. Liang, Y. Nie, X. Xu, G.-A. Yu, J. Yin, S. Hua, *Dalton Trans.* **2015**, *44*, 17473-17477; h) T. Seki, K. Kobayashi, T. Mashimo, H. Ito, *Chem. Commun.* **2018**, *54*, 11136-11139; i) F. C.-M. Leung, S. Y.-L. Leung, C. Y.-S. Chung, V. W.-W. Yam, *J. Am. Chem. Soc.* **2016**, *138*, 2889-2992; j) N.

M.-W. Wu, M. Ng, V. W.-W. Yam, *Angew. Chem. Int. Ed.* **2019**, *58*, 3027-3031; k) T. Seki, K. Ida, H. Sato, S. Aono, S. Sakaki, H. Ito, *Chem. Eur. J.* **2020**, *26*, 735-744; l) Y. Nishiuchi, A. Takayama, T. Szuki, K. Shinozaki, *Eur. J. Inorg. Chem.* **2011**, 1815-1823; m) S. J. Choi, J. Kuwabara, Y. Nishimura, T. Arai, T. Kanbara, *Chem. Lett.* **2012**, *41*, 65-67; n) X. Zhang, J.-Y. Wang, J. Ni, L.-Y. Zhang, Z.-N. Chen, *Inorg. Chem.* **2012**, *51*, 5569-5579; o) A. Han, P. Du, Z. Sun, H. Wu, H. Jia, R. Zhang, Z. Liang, R. Cao, R. Eisenberg, *Inorg. Chem.* **2014**, *53*, 3338-3344; p) A. Chowdury, P. Howlader, P. S. Mukherjee, *Chem. Eur. J.* **2016**, *22*, 1424-1434; q) C. Cuerva, J. A. Campo, M. Cano, C. Lodeiro, *Chem. Eur. J.* **2019**, *25*, 12046-12051; r) X. Zhang, L.-Y. Zhang, J.-Y. Wang, F.-R. Dai, Z.-N. Chen, *J. Mater. Chem. C* **2020**, *8*, 715-720.

[8] a) V. W.-W. Yam, V. K.-M. Au, S. Y.-L. Leung, *Chem. Rev.* **2015**, *115*, 7589-7728; b) C. Bizzarri, E. Spuling, D. M. Knoll, D. Volz, S. Bräse, *Coord. Chem. Rev.* **2018**, *373*, 48-82; c) I. O. Koshevoy, M. Krause, A. Klein, *Coord. Chem. Rev.* **2020**, *405*, 213094; d) K. Tsuge, Y. Chishina, H. Hashiguchi, Y. Sasaki, M. Kato, S. Ishizaka, N. Kitamura, *Coord. Chem. Rev.* **2016**, *306*, 636-651; e) A. Kobayashi, M. Kato, *Chem. Lett.* **2017**, *46*, 154-162; f) H. Yersin, *Highly Efficient OLEDs Materials Based on Thermally Activated Delayed Fluorescence*, Wiley-VCH, Weinheim, **2019**; g) R. Czerwieniec, M. J. Leitl, H. H. H. Homeier, H. Yersin, *Coord. Chem. Rev.* **2016**, *325*, 2-28; h) C. Lescop, *Acc. Chem. Res.* **2017**, *50*, 885-894; i) C. Lescop, *Chem. Rec.* **2021**, *21*, 544-557; j) Y. Zhang, M. Schulz, M. Wätchler, M. Karnahl, B. Dietzek, *Coord. Chem. Rev.* **2018**, *356*, 127-146; k) A. Schlachter, K. Tanner, P. D. Harvey, *Coord. Chem. Rev.* **2021**, *448*, 214176.

[9] a) B. Hupp, C. Schiller, C. Lenczyk, M. Stanoppi, K. Edkins, A. Lorbach, A. Steffen, *Inorg. Chem.* **2017**, *56*, 8996-9008; b) G. Chakkaradhari, Y.-T. Chen, A. J. Karttunen, M. T. Dau, J. Jänis, S. P. Tunik, P.-T. Chou, M.-L. Ho, I. O. Koshevoy, *Inorg. Chem.* **2016**, *55*, 2174-2184; c) R. Hamze, J. L. Peltier, D. Sylvinson, M. Jung, J. Cardenas, R. Haiges, M. Soleilhavoup, R. Jazzar, P. I. Djurovich, G. Bertrand, M. E. Thompson, *Science* **2019**, *363*, 601-606; d) S. Shi, M. C. Jung, C. Coburn, A. Tadle, D. Sylvinson M. R., P. I. Djurovich, S. R. Forrest, M. E. Thompson, *J. Am. Chem. Soc.* **2019**, *141*, 3576-3588; e) A. S. Romanov, D. Di, L. Yang, J. Fernandez-Cestau, C. R. Becker, C. E. James, B. Zhu, M. Linnolahti, D. Credgington, M. Bochmann, *Chem. Commun.* **2016**, *52*, 6379-6382; f) M. Mohankumar, F. Monti, M. Holler, F. Niess, B. Delavaux-Nicot, N. Armaroli, J.-P. Sauvage, J.-F. Nerengarten, *Chem. Eur. J.* **2014**, *20*, 12083-12090; g) M. J. Leitl, V. A. Krylova, P. I. Djurovich, M. E. Thompson, H. Yersin, *J. Am. Chem. Soc.* **2014**, *136*, 16032-16038; h) S. Keller, A. Prescimone, H. Bolink, M. Sessolo, G. Longo, L. Martinez-Sarti, J. M. Junquera-Hernandez, E. C. Constable, E. Orti, C. E. Housecroft, *Dalton Trans.* **2018**, *47*, 14263-14276; i) S. Keller, M. Bantle, A. Prescimone, E. C. Constable, C. E. Housecroft, *Molecules* **2019**, *24*, 3934; j) C. M. Brown, C. Li, V. Carta, W. Li, Z. Xu, P. H. F. Stroppa, I. D. W. Samuel, E. Zysman-Colman, M. O. Wolf, *Inorg. Chem.* **2019**, *58*, 7156-7168; k) J. Li, L. Wang, Z. Zhao, X. Li, X. Yu, P. Huo, Q. Jin, Z. Liu, Z. Bian, C. Huang, *Angew. Chem. Int. Ed.* **2020**, *59*, 8210-8217; l) M. Klein, N. Rau, M. Wende, J. Sundermeyer, G. Cheng, C.-M. Che, A. Schinabeck, H. Yersin, *Chem. Mater.* **2020**, *32*, 10365-10382; m) K. Xu, B.-L. Chen, F. Yang, L. Liu, X.-X. Zhong, L. Wang, X.-J. Zhu, F.-B. Li, W.-Y. Wong, H.-M. Qin, *Inorg. Chem.* **2021**, *60*, 4841-4851; n) J. Nitsch, F. Lacemon, A. Lorbach, A. Eichhorn, F. Cisnetti, A. Steffen, *Chem. Commun.* **2016**, *52*, 2932-2935; o) B. Huitorel, H. E. Moll, R. Utrera-Melero, M. Cordier, A. Fargues, A. Garcia, F. Massuyeau, C. Martineau-Corcos, F. Fayon, A. Rakhmatullin, S. Kahlal, J.-Y. Saillard, T. Gacoin, S. Peeruchas, *Inorg. Chem.* **2018**, *57*, 4328-4339; p) A. Kobayashi, Y. Yoshida, M. Yoshida, M. Kato, *Chem. Eur. J.* **2018**, *24*, 14750-14759; q) A. V. Artem'ev, E. A. Pritchina, M. I. Rakhmanova, N. P. Gritsan, I. Y. Bagryanskaya, S. F. Malysheva, N. A. Belogorlova, *Dalton Trans.* **2019**, *48*, 2328-2337; r) A. Y. Baranov, A. S. Berezin, D. G. Samsonenko, A. S. Mazur, P. M. Tolstoy, V. F. Plyusnin, I. E. Kolesnikov, A. V. Artem'ev, *Dalton Trans.* **2020**, *49*, 3155-3163; s) A. Kobayashi, R. Arata, T. Ogawa, M. Yoshida, M. Kato, *Inorg. Chem.* **2017**, *56*, 4280-4288; t) M. El Sayed Moussa, S. Evariste, H.-L. Wong, L. Le Bras, C. Roiland, L. Le Poles, B. Le Guennic, K. Costuas, V. W.-W. Yam, C. Lescop, *Chem. Commun.* **2016**, *52*, 11370-11373; u) S. Bassoli, G. Attilio Ardizzoia, B. Therrien, S. Brenna, *Dalton Trans.* **2019**, *48*, 9276-9283; v) F. Moutier, J. Schiller, G. Calvez, C. Lescop, *Org. Chem. Front.* **2021**, *8*, 2893-2902; w) S. Chen, J. Gao, J. Chang, Y. Li, C. Huangfu, H. Meng, Y. Wang, G. Xia, L. Feng, *ACS Appl. Mater. Interfaces* **2019**, *11*, 17513-17520; x) C. Sun, L. Llanos, P. Aroe, A. Oliver, R. Wannemacher, J. Cabanillas-Gonzalez, L. Lemus, D. Aravena, *Chem. Mater.* **2021**, *33*, 6383-6393.

[10] a) T. Hasegawa, A. Kobayashi, H. Ohara, M. Yoshida, M. Kato, *Inorg. Chem.* **2017**, *56*, 4928-4936; b) B. Hupp, J. Nitsch, T. Schmitt, R. Bertermann, K. Edkins, F. Hirsch, I. Fischer, M. Auth, A. Sperlich, A. Steffen, *Angew. Chem. Int. Ed.* **2018**, *57*, 13671-13675; c) C. Li, W. Li, A. F. Henwood, D. Hall, D. B. Cordes, A. M. Z. Slawin, V. Lemaur, Y. Olivier, I. D. W. Samuel, E. Zysman-Colman, *Inorg. Chem.* **2020**, *59*, 14772-14784; d) T. Hayashi, A. Kobayashi, H. Ohara, M. Yoshida, T. Matsumoto, H.-C. Chang, M. Kato, *Inorg. Chem.* **2015**, *54*, 8905-8913; e) Q. Benito, C. M. Balogh, H. El Moll, T. Gacoin, M. Cordier, A. Rakhmatullin, C. Latouche, C. Martineau-Corcos, S. Perruchas, *Chem. Eur. J.* **2018**, *24*, 18868-18872; f) Z.-C. Shi, W. Chen, S.-Z. Zhan, M. L, M. Xie, Y. Y. Li, S. W. Ng, Y.-L. Huang, Z. Zhang, G.-H. Ning, D. Li, *Inorg. Chem. Front.* **2020**, *7*, 1437-1444; g) S. Perruchas, X. F. Le Goff, S. Maron, I. Maurin, F. Guillen, A. Garcia, T. Gacoin, J.-P. Boilot, *J. Am. Chem. Soc.* **2010**, *132*, 10967-10969; h) Q. Benito, X. F. Le Goff, S. Maron, A. Fargues, A. Garcia, C. Martineau, F. Taulelle, S. Kahlal, T. Gacoin, S. Perruchas, *J. Am. Chem. Soc.* **2014**, *136*, 11311-11320; i) S. Evariste, A. M. Khalil, S. Kerneis, C. Xu, G. Calvez, K. Costuas, C. Lescop, *Inorg. Chem. Front.* **2020**, *7*, 3402-3411; j) S. Ogawa, H. Katsuragi, T. Ikeda, K. Oshima, S. Satokawa, Y. Yamazaki, T. Tsubomura, *Dalton Trans.* **2021**, *50*, 8845-8850.

[11] N. V. S. Harisomayajula, S. Makovetskyi, Y.-C. Tsai, *Chem. Eur. J.* **2019**, *25*, 8936-8954

[12] a) R. Utrera-Melero, B. Huitorel, M. Cordier, J.-Y. Mevellec, F. Massuyeau, C. Latouche, C. Martineau-Corcos, S. Perruchas, *Inorg. Chem.* **2020**, *59*, 13607-13620; b) R. Utrera-Melero, B. Huitorel, M. Cordier, F. Massuyeau, J.-Y. Mevellec, N. Stephant, P. Deniard, C. Latouche, C. Martineau-Corcos, S. Perruchas, *J. Mater. Chem. C* **2021**, *9*, 7991-8001.

[13] a) X.-W. Chen, L.-H. He, P. Ju, J.-L. Chen, S.-J. Liu, H.-R. Wen, *J. Mater. Chem. C* **2020**, *8*, 16160-16167; b) X. Yu, X. Li, Z. Cai, L. Sun, C. Wang, X. Rao, C. Wei, Z. Bian, Q. Jin, Z. Liu, *Chem. Commun.* **2021**, *57*, 5082-5085.

[14] A. Y. Baranov, E. A. Pritchina, A. S. Berezin, D. G. Samsonenko, V.P. Fedin, N. A. Belogorlova, N. P. Gritsan, A. V. Artem'ev, *Angew. Chem. Int. Ed.* **2021**, *60*, 12577-12584.

[15] S. Evariste, A. M. Khalil, M. El Sayed Moussa, A. K.-W. Chen, E. Y.-H. Hong, H.-L. Wong, B. Le Guennic, G. Calvez, K. Costuas, V. W.-W. Yam, C. Lescop, *J. Am. Chem. Soc.* **2018**, *140*, 12521-12526.

[16] a) M. El Sayed Moussa, A. M. Khalil, S. Evariste, H.-L. Wong, V. Delmas, B. Le Guennic, G. Calvez, K. Costuas, V. W.-W. Yam, C. Lescop, *Inorg. Chem. Front.* **2020**, *7*, 1334-1344; b) A. M. Khalil, C. Xu, V. Delmas, G. Calvez, K. Costuas, M. Haouas, C. Lescop, *Inorg. Chem. Front.* **2021**, DOI : 10.1039/D1QI00937K.

[17] Equal relative occupancies for C and N atoms have been modelled at the atomic position determined for the cyano ligands connecting two Cu(I) metal centers. For the $Pd(CN)_4$ fragments, C atoms have been assigned to the atoms connected to the Pd(II) metal centres. See SI for more information.

[18] Temperature-dependent X-ray crystal structure analyses were performed on the same single crystals of $\mathbf{B_c}$ at 250 K, 200 K, 150 K, and 100 K. The structural data reveal a moderate shrinkage of the unit cell volume upon cooling but there is no marked alteration of the metric parameters concerning the metal centres and the metallacycle, revealing the structural rigidity of this assembly. See SI for more information.

[19] For experimental details, spectroscopic, X-ray diffraction data and computational studies, see SI.

[20] Grinding process applied on $\mathbf{B_o}$ samples, affording $\mathbf{B_g}$ samples, were applied several times, affording independent batches whose photophysical properties were comparable.

[21] Recrystallizations conducted from dissolved phases $\mathbf{B_g}$ and $\mathbf{B_m}$ always yielded single-crystals of $\mathbf{B_o}$, supporting the hypothesis that multiple

and complex fast equilibria based on intramolecular exchanges occur in solution at RT, allowing easy interconversion between the conformers.

Entry for the Table of Contents

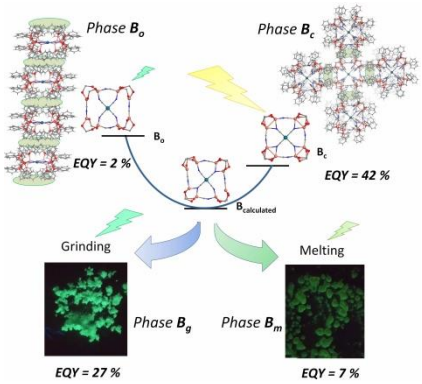

A combined experimental and computational study highlights the crucial role played by intermolecular non-covalent weak-interactions in the conformer selection, the solid-state organization and the photophysical properties observed in a series of phases of a $Cu^{I}_{8}Pd^{II}_{2}$ multimetallic assembly. Rationalization of the structure/properties relationships allows understanding their mechanical and thermal stimuli-sensitive responses.

Institute and/or researcher Twitter usernames: @chimie_ISCR